

Structural and Magnetic Properties of Mo-Zn Substituted ($\text{BaFe}_{12-4x}\text{Mo}_x\text{Zn}_{3x}\text{O}_{19}$) M-type Hexaferrites

S.H. MAHMOOD^{1*}, A. N. ALOQAILY¹, Y. MASWADEH¹,
A. AWADALLAH¹, I. BSOUL² and H. JUWHARI¹

¹Department of Physics, The University of Jordan, Amman 11942, Jordan.

²Department of Physic, Al al-Bayt University, Mafraq 13040, Jordan.

<http://dx.doi.org/10.13005/msri/110102>

(Received: August 23, 2014; Accepted: September 02, 2014)

ABSTRACT

Molybdenum-zinc substituted hexaferrites were synthesized by high-energy ball milling and subsequent sintering at different temperatures (1100, 1200, and 1300° C). The samples sintered at 1100° C exhibited good hard magnetic properties, although a decrease in saturation magnetization from 70.2 emu/g for the unsubstituted sample down to 57 emu/g for the sample with $x = 0.3$ was observed. The drop in saturation magnetization results mainly from the presence of secondary nonmagnetic oxides. The samples sintered at temperatures $\geq 1200^\circ\text{C}$ showed an improvement in saturation magnetization, and a sharp drop in coercivity. This behavior was associated with the development of the W-type hexaferrite, the particle growth, and possibly the spin reorientation transition from easy-axis to easy-plane.

Key words: Hexaferrites; Magnetic properties; Structural analysis.

INTRODUCTION

Magnetic materials play a crucial role in our everyday life. Permanent magnets produced from hard magnetic materials are found in home appliances such as TVs, audio systems, computers, phones, speakers, etc. The number of permanent magnets in our vehicles, for example, had grown in the recent years with the increasing demand for additional motors required for applications in starters and window lifters. Other soft magnetic materials are in transformers, power supplies, and electronic components for telecommunication applications. The wide range of applications of magnetic materials with different magnetic and physical characteristics had therefore generated a great interest in the fabrication and characterization of new magnetic materials. In this context, fabrication techniques, experimental conditions and chemical

compositions of various ferrites were controlled to obtain materials with desirable properties for a wide range of applications¹⁻³.

Hexagonal ferrites (or simply, hexaferrites) form a class of magnetic materials of central importance due to their properties which can be tailored to suite specific industrial and technological applications, simple fabrication processes, chemical and thermal stability, and low cost. These ferrimagnetic oxides with hexagonal structure have a wide range of applications in permanent magnet industry, microwave devices, catalysis, and magnetic recording and data storage¹⁻¹⁰.

M-type barium hexaferrite (also known as Ferroxdure or BaM) is a ferrimagnetic material with a melting point of 1390 °C, molecular mass 1112 g, maximum density $\rho = 5.295\text{ g/cm}^3$ and coercivity

of 160–255 kA m⁻¹. BaMhexaferrite is the most important hexaferrite in terms of production (more than 50% of the total globally manufactured magnetic materials [4]).

The unit cell of M-type barium hexaferrite is built by stacking R (BaFe₆O₁₁) and S (Fe₆O₈) blocks in the sequence RSR*S*, where the star denotes a block rotated by 180° about the *c*-axis of the hexagonal lattice [4]. The unit cell therefore contains two (BaFe₁₂O₁₉) molecules. The S block contains two hexagonal layers of four oxygen ions in each, while the R block consists of three hexagonal oxygen layers, with one oxygen ion in the middle layer replaced substitutionally by a Ba ion. The metal ions occupy five different interstitial sites: two sites in the S block (the octahedral 2*a* site and the tetrahedral 4*f*₁ site), two sites in the R block (the octahedral 4*f*₂ site and the by-pyramidal 2*b* site) and one site at the R-S interfaces (the 12*k* octahedral site). These sublattices, their coordinations, the number of metal ions in each, and their spin directions are listed in Table 1.

Precursor powders of barium hexaferrites were prepared by various workers using different methods of preparation such as hydrothermal synthesis¹¹, sol-gel method^{12,13}, wet chemical method¹⁴, ball milling¹⁵⁻²¹, nitrate–citrate gel^{22, 23}, and chemical coprecipitation^{24,25}.

The magnetic and electrical properties of barium hexaferrites were found to depend critically on the substitution of barium ions or iron ions by other cations and cations combinations. Trivalent metal ions, or combinations of divalent and tetravalent ions were used to substitute Fe³⁺ ions in the hexaferrite lattice. These included Al^{15, 19,26}, Ga^{19,27}, (Mo_{*x*}Zn_{*0.4-x*})¹⁴, Mn¹², Cr¹⁹, Ti-Ru¹⁶, Zn–Ti¹³, and Sn-Ru¹⁸.

In the present work, we synthesized barium hexaferrites with Fe ions partially substituted by Mo⁶⁺–Zn²⁺ combinations. In order to maintain the cationic valence states the ratio of Mo:Zn was fixed at 1:3. The effects of the type of substitution and substitution level, and heat treatment on the structural, magnetic and physical properties of the prepared samples were investigated using x-ray diffraction (XRD), scanning electron microscopy (SEM), and vibrating sample magnetometry (VSM).

The structural refinement for the prepared samples was achieved using FULLPROF software based on Rietveld refinement techniques.

EXPERIMENTAL

High purity (~99%) powders of BaCO₃, Fe₂O₃, ZnO and MoO₂ were used as starting materials to prepare the powder precursors of Mo–Zn substituted (BaFe_{12-4*x*}Mo_{*x*}Zn_{3*x*}O₁₉)M-type hexaferrites. The barium to metal molar ratio was 1:11, and the molybdenum to zinc ratio was 1:3. Since zinc is divalent, the substitution of this combination for Fe³⁺ ions in these hexaferrites ensures that molybdenum has the Mo⁶⁺ valence state, which ensures the chemical neutrality of the hexaferrite.

The required amounts of the starting powders were weighed accurately and then mixed and transferred to the zirconia milling vessels. The mixture was then milled in an acetone bath (8 ml for each 5 grams of the powder) for 16 hours. The milling time was sectioned into 10 min. grinding periods interrupted by 5 min. pause periods to allow for cooling the sample and avoid overheating. The ball-to-powder mass ratio was 14:1 and the rotation speed was 250 rpm. The resulting wet powder mixture was left in the container overnight to dry at room temperature, and then the dry powder was collected in clean glass vials. An adhesive agent of aqueous solution of 2% wt. of polyvinyl alcohol (PVA) was prepared and transferred to the vial containing the milled powder and thoroughly mixed with the powder. After drying at room temperature, parts of the powder (about 1 gram each) were pressed into a disc (1.5 cm in diameter) in a stainless steel die under a 4 ton force. The discs were subsequently sintered at temperatures in the range 1100 – 1300°C.

The density for each disc was calculated by dividing the mass of the disk by its volume, and found to be independent on the level of substitution (2.7 ± 0.1 g/cm³ for all samples sintered at 1100°C). However, we noticed a tendency toward increasing the density with increasing sintering temperature, where the average density of the discs sintered at 1200°C increased to about 3.0 ± 0.1 g/cm³ and that for discs sintered at 1300°C increased up to about 3.3 ± 0.05 g/cm³. This behavior could be attributed to the growth in particle size with increasing the

sintering temperature, which in turn reduces the porosity of the samples.

Scanning electron microscope (SEM) system (FEI-Inspect F50/FEG) was used to investigate the microstructural characteristics of the samples. The chemical compositions of the samples were determined using the energy dispersive x-ray spectroscopy (EDX) facility available in the SEM system.

The structural characteristics of the samples were investigated using x-ray diffraction (XRD). XRD patterns of the samples were obtained in the angular range 20° – 70° using XRD 7000-Shimadzu machine with Cu-K α radiation. The scanning step was 0.02° and the scanning rate was 1deg/min. The patterns were then analyzed using dedicated software routines (FULLPROF and Expert High Score) to determine the structural parameters of the samples.

The coercivity (H_c), remnant magnetization (M_r) and saturation magnetization (M_s) of the samples were determined from the hysteresis loops measured using a standard vibrating sample magnetometer (VSM Micro Mag 3900, Princeton Measurements Corporation). All magnetic measurements were performed at room temperature in an applied field up to 10 kOe.

RESULTS

Analysis

Scanning electron microscopy (SEM)

Fig. 1 shows SEM images for the samples at T = 1100° C. The images indicate that the particle size and morphology does not seem to be influenced by the substitution, and show hexagonal platelets with diameters ranging from 200 nm to about 500nm for all samples under investigation. However, lighter particles with generally smaller size and different morphology was also observed, which gave the impression that we may have different phases in the samples. This was examined by EDX analysis of the spectra collected at darker (D) and lighter (L) particles of the sample with x = 0.2 (BaFe_{11.2}Mo_{0.2}Zn_{0.6}O₁₉) as an example (Fig. 2). The atomic Ba:Fe ratio in the darker particles was found to be 1:12.2 which is close to the stoichiometric ratio of BaFe₁₂O₁₉. On the other hand, the Ba:Mo ratio in the lighter particles was 1:1.07, which is consistent with the stoichiometric ratio of BaMoO₄. These results indicate that the Mo–Zn substituted samples with BaM stoichiometry may contain a secondary barium molybdenum oxide phase coexisting with the hexaferrite major phase under these experimental conditions.

Table 1: Metallic sub-lattices of M-type hexaferrite

| Block | sublattice | Coordination | Ions per unit cell | Spin direction |
|-------|-----------------|--------------|--------------------|----------------|
| S | 4f ₁ | Tetrahedral | 4 | down |
| | 2a | Octahedral | 2 | Up |
| R | 4f ₂ | Octahedral | 4 | Down |
| | 2b | Bi-pyramidal | 2 | Up |
| S-R | 12k | Octahedral | 12 | Up |

Table 2: Lattice parameters (a and c), cell volume V, Bragg R-factor and RF-factor for BaFe_{12-4x}Mo_xZn_{3x}O₁₉ samples sintered at 1100° C

| x | Chemical formula of sample | χ^2 | V (Å ³) | a = b (Å) | c (Å) | Bragg R-factor | RF-factor |
|------|--|----------|---------------------|-----------|---------|----------------|-----------|
| 0.0 | BaFe ₁₂ O ₁₉ | 1.24 | 696.3127 | 5.8899 | 23.2066 | 0.440 | 0.600 |
| 0.1 | BaFe _{11.6} Mo _{0.1} Zn _{0.3} O ₁₉ | 1.15 | 698.0667 | 5.8923 | 23.2167 | 0.792 | 0.936 |
| 0.15 | BaFe _{11.4} Mo _{0.15} Zn _{0.45} O ₁₉ | 1.23 | 697.6312 | 5.8917 | 23.2069 | 0.545 | 0.619 |
| 0.2 | BaFe _{11.2} Mo _{0.2} Zn _{0.6} O ₁₉ | 1.074 | 698.4347 | 5.8933 | 23.2206 | 0.905 | 0.594 |
| 0.3 | BaFe _{10.8} Mo _{0.3} Zn _{0.9} O ₁₉ | 1.19 | 698.1218 | 5.8931 | 23.2119 | 0.605 | 0.566 |

This method, although does not provide an accurate quantitative analysis of the compositions of the samples due to the low concentrations of some elements in comparison with the experimental uncertainty of the technique, it is useful in checking for the possibility of having secondary phases.

Table 3: Cell volume V_c and crystal size for $\text{BaFe}_{12-4x}\text{Mo}_x\text{Zn}_{3x}\text{O}_{19}$ s sintered at 1100° C

| x | Chemical formula of ferrite | V_c (Å ³) | χ^2 | D(nm) |
|-----|---|-------------------------|----------|-------|
| 0 | $\text{BaFe}_{12}\text{O}_{19}$ | 696.3 | 1.24 | 14.6 |
| 0.1 | $\text{BaFe}_{11.6}\text{Mo}_{0.1}\text{Zn}_{0.3}\text{O}_{19}$ | 698.0 | 1.15 | 10.7 |
| 0.2 | $\text{BaFe}_{11.2}\text{Mo}_{0.2}\text{Zn}_{0.6}\text{O}_{19}$ | 698.4 | 1.07 | 9.1 |

Table 4: Cell volume V , Bragg R-factor and RF-factor of the BaM phase in two different samples sintered at 1100 and 1200° C

| x | Chemical formula of samples | T | χ^2 | V | Bragg R-factor | RF-factor |
|------|---|------|----------|---------|----------------|-----------|
| 0.15 | $\text{BaFe}_{11.6}\text{Mo}_{0.1}\text{Zn}_{0.3}\text{O}_{19}$ | 1100 | 1.23 | 697.631 | 0.545 | 0.619 |
| 0.15 | $\text{BaFe}_{11.6}\text{Mo}_{0.1}\text{Zn}_{0.3}\text{O}_{19}$ | 1200 | 1.28 | 696.620 | 0.878 | 0.668 |
| 0.2 | $\text{BaFe}_{11.2}\text{Mo}_{0.2}\text{Zn}_{0.6}\text{O}_{19}$ | 1100 | 1.074 | 698.435 | 0.905 | 0.594 |
| 0.2 | $\text{BaFe}_{11.2}\text{Mo}_{0.2}\text{Zn}_{0.6}\text{O}_{19}$ | 1200 | 1.37 | 697.973 | 1.280 | 0.857 |

Table 5: Cell volume V_c , Bragg R-factor and RF-factor for $\text{BaFe}_{11.4}\text{Mo}_{0.15}\text{Zn}_{0.45}\text{O}_{19}$ at different temperature

| Chemical formula of ferrite | Temp. | Number of phases: | χ^2 | V_c | Bragg R-factor | RF-factor | |
|---|-------|-------------------|--|-------|----------------|-----------|-------|
| $(\text{BaFe}_{11.4}\text{Mo}_{0.15}\text{Zn}_{0.45}\text{O}_{19})$ | 1100 | 3 | $\text{BaFe}_{12}\text{O}_{19}$ | 1.23 | 697.63 | 0.545 | 0.619 |
| | | | BaMoO_4 | | 398.26 | 0.529 | 0.546 |
| | | | ZnFe_2O_4 | | 599.55 | 0.699 | 0.632 |
| | 1200 | 3 | $\text{BaFe}_{12}\text{O}_{19}$ | 1.28 | 696.62 | 0.878 | 0.665 |
| | | | BaMoO_4 | | 396.85 | 0.830 | 0.674 |
| | | | $\text{BaZn}_2\text{Fe}_{16}\text{O}_{27}$ | | 997.37 | 0.887 | 0.825 |
| | 1300 | 3 | $\text{BaFe}_{12}\text{O}_{19}$ | 1.45 | 703.65 | 0.781 | 0.690 |
| | | | BaMoO_4 | | 399.10 | 1.020 | 0.686 |
| | | | $\text{BaZn}_2\text{Fe}_{16}\text{O}_{27}$ | | 997.46 | 0.645 | 0.429 |

Table 6: Saturation magnetization (M_s), remnant magnetization (M_r), coercivity (H_c) and squareness ratio (M_r/M_s) of $\text{BaFe}_{12-4x}\text{Mo}_x\text{Zn}_{3x}\text{O}_{19}$ samples sintered at 1100° C

| Concentration (x) | Chemical formula of sample | M_s (emu/g) | H_c (Oe) | M_r (emu/g) | M_r/M_s |
|-----------------------|---|---------------|------------|---------------|-----------|
| 0.0 | $\text{BaFe}_{12}\text{O}_{19}$ | 70.2 | 3455 | 40.6 | 0.58 |
| 0.1 | $\text{BaFe}_{11.6}\text{Mo}_{0.1}\text{Zn}_{0.3}\text{O}_{19}$ | 69.4 | 2594 | 37.2 | 0.53 |
| 0.15 | $\text{BaFe}_{11.4}\text{Mo}_{0.15}\text{Zn}_{0.45}\text{O}_{19}$ | 63.6 | 2729 | 34.5 | 0.54 |
| 0.2 | $\text{BaFe}_{11.2}\text{Mo}_{0.2}\text{Zn}_{0.6}\text{O}_{19}$ | 58.9 | 2793 | 31.3 | 0.53 |
| 0.3 | $\text{BaFe}_{10.8}\text{Mo}_{0.3}\text{Zn}_{0.9}\text{O}_{19}$ | 57.0 | 2790 | 30.5 | 0.54 |

Table 7: Saturation magnetization (M_s), remnant magnetization (M_r), coercivity (H_c), and squareness ratio (M_r/M_s) values of ferrite samples with $x = 0.2$ sintered at different sintering temperatures (T_s)

| T_s | x | Chemical formula | M_s (emu/g) | H_c (Oe) | M_r (emu/g) | M_r/M_s |
|-------|-----|--|---------------|------------|---------------|-----------|
| 1100 | 0.2 | BaFe _{11.2} Mo _{0.2} Zn _{0.6} O ₁₉ | 58.9 | 2793 | 31.3 | 0.53 |
| 1200 | 0.2 | BaFe _{11.2} Mo _{0.2} Zn _{0.6} O ₁₉ | 65.0 | 829 | 27.2 | 0.41 |
| 1300 | 0.2 | BaFe _{11.2} Mo _{0.2} Zn _{0.6} O ₁₉ | 70.5 | 308 | 12.2 | 0.15 |

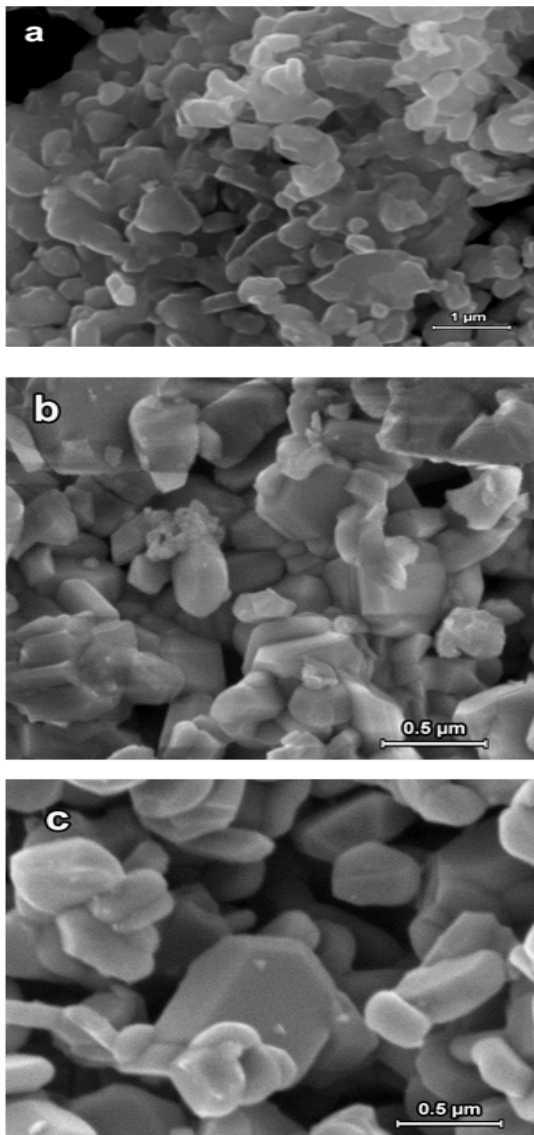


Fig. 1: SEM images of samples sintered at 1100° C with Mo concentration (a) $x = 0.0$, (b) $x = 0.1$, and (c) $x = 0.2$

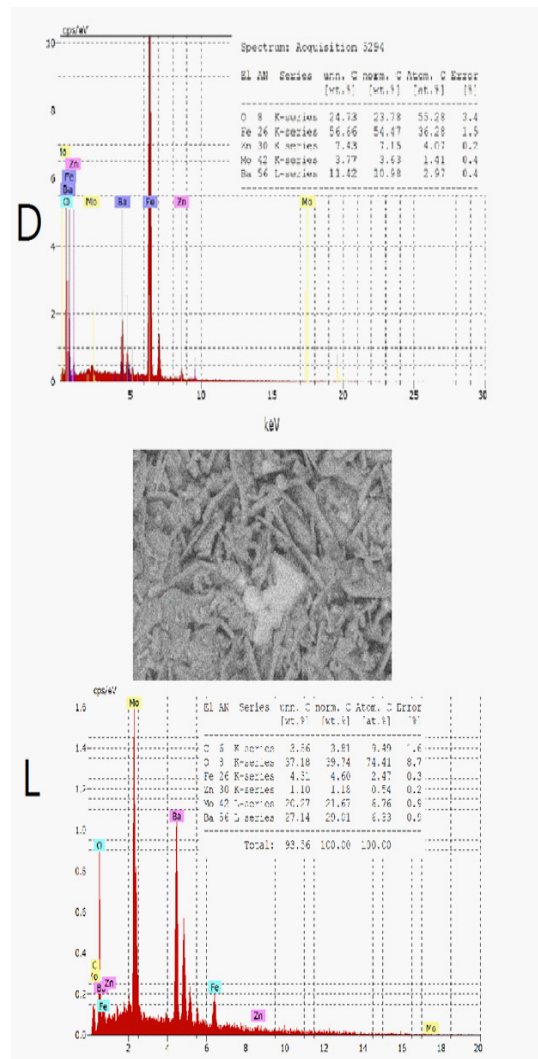


Fig. 2: EDX patterns for darker (D) and lighter (L) particles of BaFe_{11.2}Mo_{0.2}Zn_{0.6}O₁₉ sintered at 1100° C

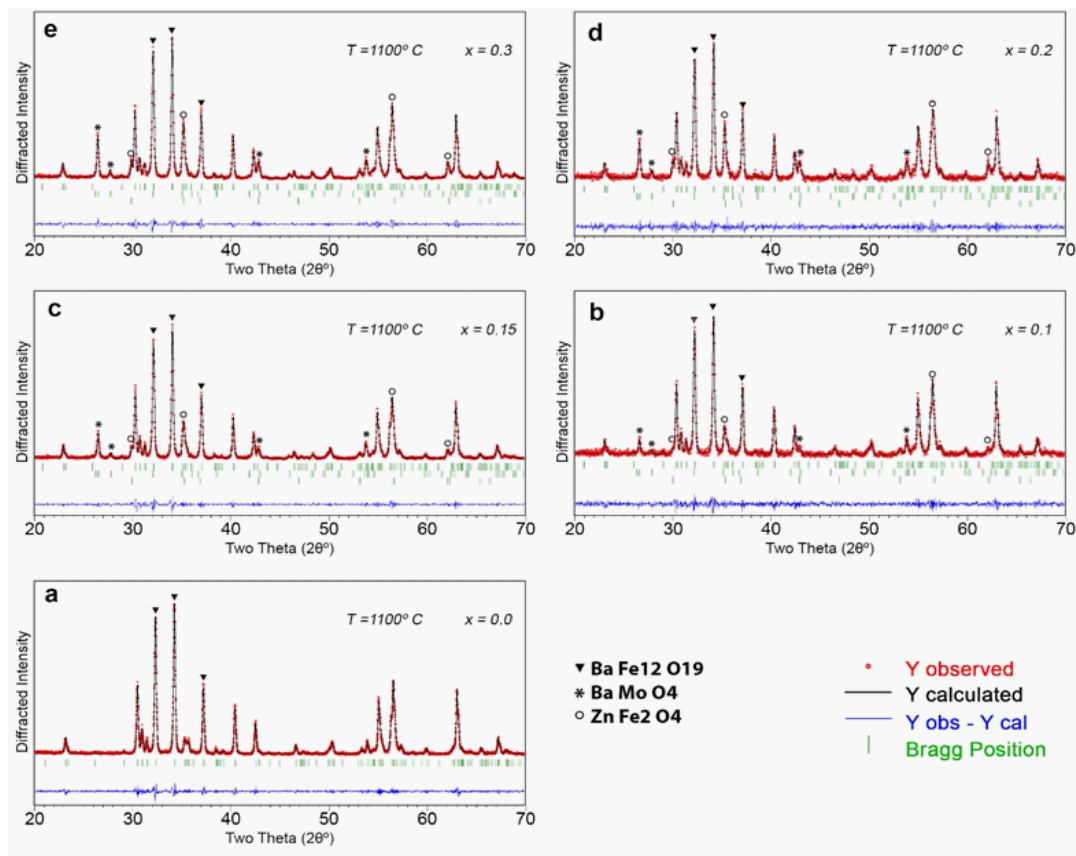


Fig. 3: Refined XRD patterns for all BaFe_{12-4x}Mo_xZn_{3x}O₁₉ hexaferrites sintered at 1100°C

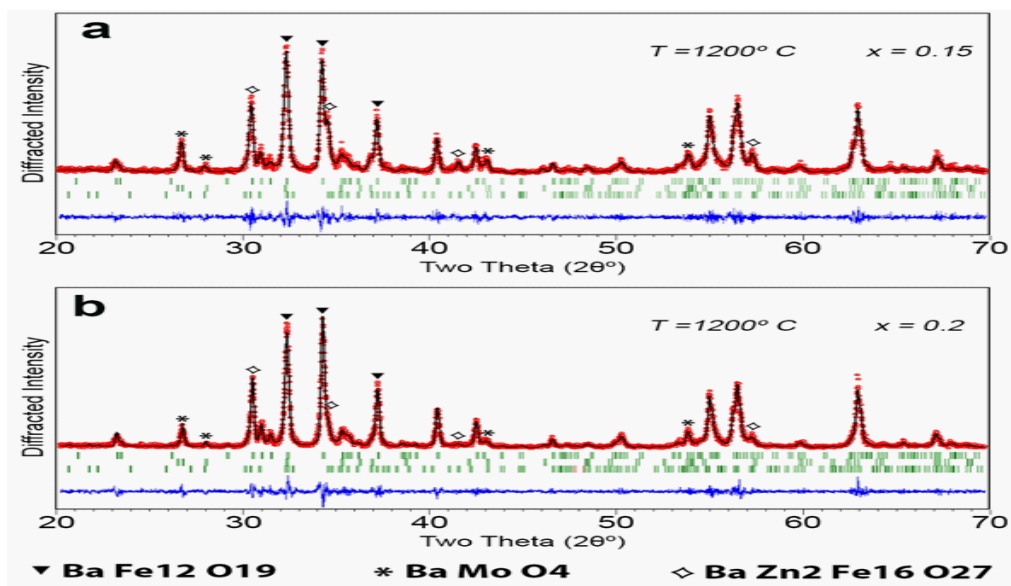


Fig. 4: FULLPROF refined XRD patterns for BaFe_{12-4x}Mo_xZn_{3x}O₁₉ with different Mo concentrations (x = 0.15 and 0.2) sintered at 1200°C

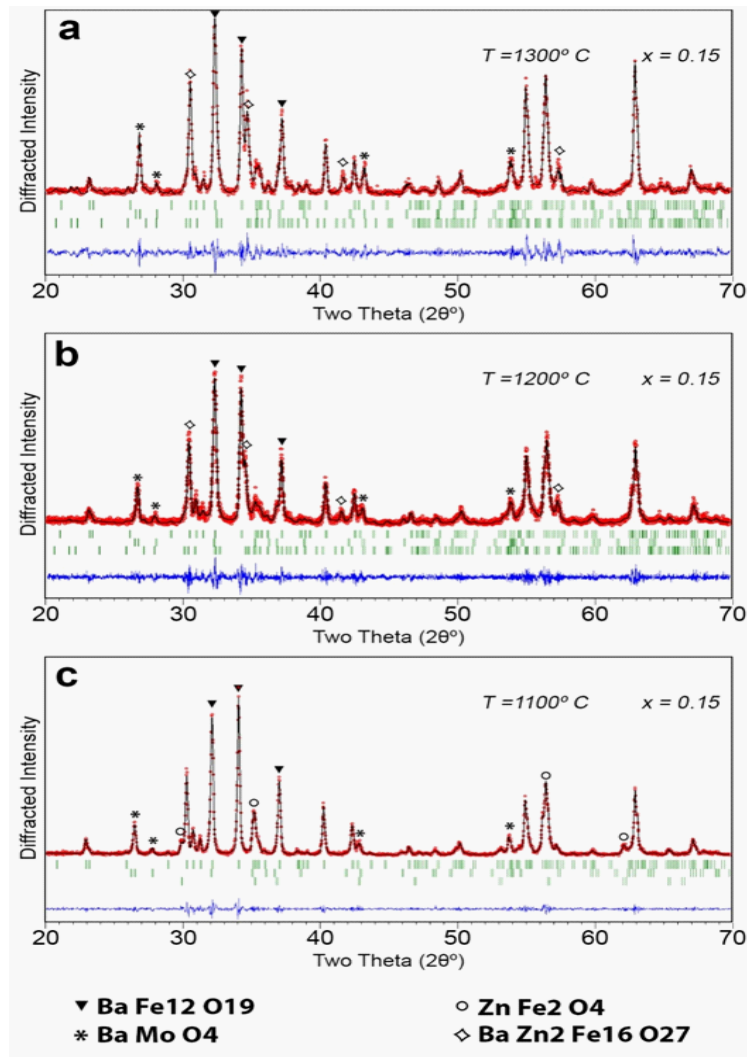


Fig. 5: FULLPROF refined XRD patterns for $\text{BaFe}_{11.4}\text{Mo}_{0.15}\text{Zn}_{0.45}\text{O}_{19}$ at different sintering temperature

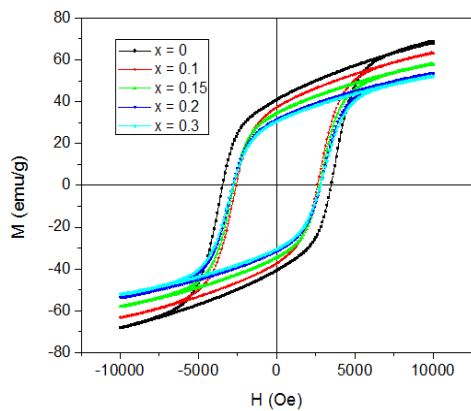


Fig. 6: Hysteresis loops of $\text{BaFe}_{12-4x}\text{Mo}_{3x}\text{Zn}_{3x}\text{O}_{19}$ samples sintered at 1100°C

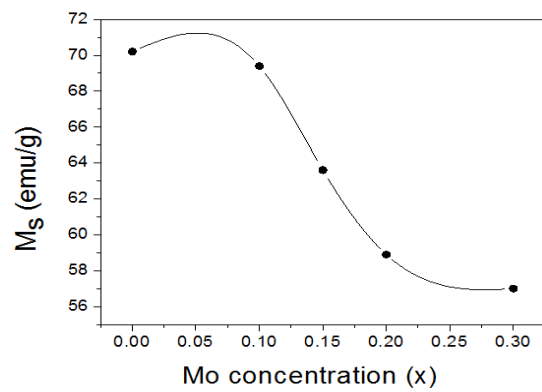


Fig. 7: Saturation magnetization of $\text{BaFe}_{12-4x}\text{Mo}_{3x}\text{Zn}_{3x}\text{O}_{19}$ as a function of Mo concentration x

Therefore, a detailed structural analysis is required to identify the existing phases and their structural properties.

X-ray diffraction (XRD) measurements

Figure 3 shows the XRD patterns for all samples sintered at 1100° C. The figure indicates the development of new phases with increasing x values as evidenced by the peaks around 26.6°, 30.0°, and 35.03°. The diffraction patterns were analyzed using FULLPROF software. The pattern for the un-doped sample shows a major phase with reflections consistent with BaFe₁₂O₁₉ M-type hexaferrite (JCPDS: 00-043-0002) without other impurity phases. On the other hand, XRD patterns indicate that all doped samples consist of a major BaM hexaferrite phase and small amounts of other intermediate phases (ZnFe₂O₄ and BaMoO₄). The formation of BaMoO₄ phase which is consistent with the results of EDX analysis, causes deficiency in the amount of Ba (or excessive amounts of Fe and Zn) required for BaM phase, resulting in the formation of ZnFe₂O₄ phase.

A large number of parameters can be obtained directly from the refinement routine such as the lattice constants (a and c), cell volume V , Miller indices of the diffraction peaks (hkl), and the goodness of fit parameters. Some refined parameters resulting from fitting the experimental diffraction data are shown in Table 2. The refinement results indicate slight fluctuations of the lattice constants around $a = 5.89$ Å and $c = 23.21$ Å. The

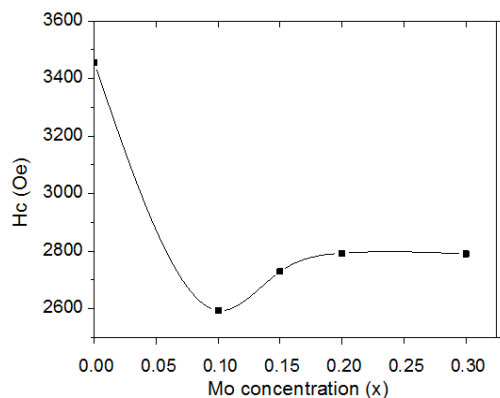


Fig. 8: Coercivity of BaFe_{12-4x}Mo_xZn_{3x}O₁₉ sintered at 1100° C as a function of Mo concentration (x)

slight increase in cell volume upon substitution of iron by zinc and molybdenum could be due to partial substitution of the larger Zn²⁺ ions (radius = 0.74 Å) for the smaller Fe³⁺ ions (radius = 0.49 Å) at the 4f₁ tetrahedral sites²⁸.

In order to investigate the effect of compaction on the development of phases and crystallinity, samples in powder form were sintered at 1100° C and investigated by XRD. The refinement results indicated that these patterns are almost identical to those for disk-sintered samples, which indicates that the compaction of the powder under a 4-ton pressure did not influence the phase evolution in the samples.

The average crystallite size for each sample was calculated from the Scherrer equation [29]:

$$D = \frac{k\lambda}{\beta \cos(\theta)}$$

where k is a constant equals 0.9, $\lambda = 1.542$ Å, β is the peak-width at half maximum, and θ is the angular position of the peak. The average crystallite sizes for the investigated samples with x ranging from 0.0 to 0.2 are listed in Table 3. The data indicates that the crystallite size tends to decrease from about 15 nm down to about 9 nm with increasing x . This leads to the conclusion that the Mo–Zn substitution for Fe results in poorer crystallinity of the samples, probably arising from crystal defects.

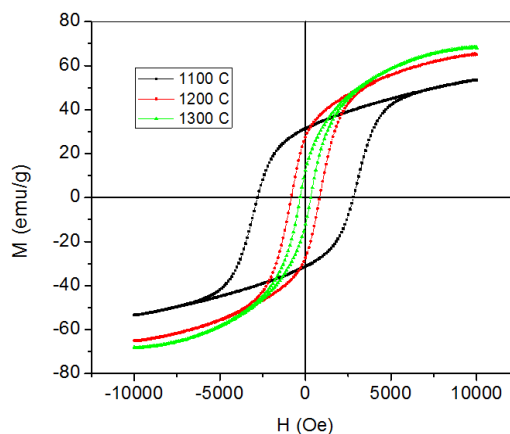


Fig. 9: Hysteresis loops of aFe_{11.2}Mo_{0.2}Zn_{0.6}O₁₉ sintered at 1100, 1200, and 1300° C

To examine the effect of sintering temperature on the structure of the ferrites, all samples were resintered at 1200° C for 2 h, and their structure investigated by XRD. Fig. 4 shows X-ray patterns for resintered samples. The patterns clearly indicate that ZnFe₂O₄ phase disappeared in the samples, while the BaMoO₄ phase persisted throughout the whole concentration range and a new high-temperature phase evolved, which was identified as W-type BaZn₂Fe₁₆O₂₇(Zn₂W) phase. Bearing in mind that the unit cell of the W-type phase is a combination of the unit cell of BaM and a spinel (Zn₂Fe₄O₈) block, this phase apparently evolved according to the reaction:



The structural parameters for the M-type phase in these samples were derived from the FULLPROF analysis and listed in Table 4. The data indicate slight decrease in cell volume toward that of the un-substituted sample with increasing the sintering temperature. This is associated with the incorporation of Zn²⁺ ions in the evolving Zn₂W hexaferrite rather than in the BaM hexaferrite lattice. To further investigate the effect of sintering temperature, the sample with $x = 0.15$ (BaFe_{11.4}Mo_{0.15}Zn_{0.45}O₁₉) was re-sintered at a temperature 1300° C and the patterns for this sample at different temperature are shown in Fig. 5. It is evident that the BaMoO₄ phase existed at all temperatures, while ZnFe₂O₄ disappeared completely at temperatures higher than 1200° C. At such high sintering temperatures, the reaction between the (intermediate) M-type and spinel phases is completed to form the Zn₂W-type phase. Thus, we conclude that the reaction the M-type phase and the zinc spinel Zn₂Fe₄O₈ (S) phase is favored at high temperatures (~1300° C). Our results are consistent with previously reported results³⁰, which indicated the presence of M-phase at low sintering temperatures, and the development of the W-phase at temperatures higher than 1200° C.

Magnetic measurements

Fig. 6 shows the hysteresis curves for BaFe_{12-4x}Mo_xZn_{3x}O₁₉ samples sintered at 1100° C. The curves indicate that the magnetizations do not saturate in the magnetic field range of the study. According to the law of approach to saturation, the

magnetization in the high field region is dominated by magnetic domain rotation¹. Therefore, this law was used to determine the saturation magnetization for each sample from the high field region ($H > 0.8$ kOe), while the coercivity and remnant magnetization were determined directly from the hysteresis loops, and the results are listed in Table 6.

As shown in Table 6 the saturation magnetization for the un-substituted sample is 70.2 emu/g, the remnant magnetization is 40.6 emu/g. The squareness ratio of about 0.58 for this sample is close to the value (0.5) for a system of randomly oriented single domain particles³. The saturation magnetization (Fig. 7) decreased gradually with increasing Mo concentration, recording a 19% drop in the sample with $x = 0.3$. However, the magnetic properties of the products are still good for permanent magnet or data storage applications.

The initial drop in coercivity (Fig.8) of about 25% for the sample with $x = 0.1$ is consistent with previously reported results¹⁴. This behavior was associated with the substitution of the Fe³⁺ ions by Zn²⁺ ions at 4f₁ sites and Mo⁶⁺ ions at 2b sites (which have the highest contribution to the magnetic anisotropy). The progressive increase of Zn²⁺ ions at 4f₁ sites and Mo⁶⁺ ions at spin-up 2b sites is expected to result in an increase in the saturation magnetization and a further drop in coercivity, contrary to observed results. Therefore, we associate the noticeable decrease in saturation magnetization and the almost constant value of the coercivity with increasing x to the limited solubility of Zn – Mo ions in the BaM lattice, and the development of the non-magnetic (ZnFe₂O₄ and BaMoO₄) oxide phases, which influence the saturation magnetization, but not the coercivity. In view of the reduction of the saturation magnetization for the sample with $x = 0.3$, the nonmagnetic oxides apparently account for 19% of the sample weight.

It is well known that the sintering temperature has an important effect on the magnetic properties, especially on the coercivity value, which is sensitive to the grain morphology^{3,31,32}. The hysteresis loops for samples with $x = 0.2$ sintered at different temperatures are shown in Fig. 9. The magnetic parameters derived from these loops are listed in Table 7. The increase in saturation magnetization

with increasing sintering temperature is associated with the disappearance of the nonmagnetic ZnFe_2O_4 phase and the development of the W-phase. Such structural developments were not observed in Mo–Zn substituted hexaferrites prepared by wet chemical mixing with different Mo to Zn ratio^{14, 33}. The sharp drop of the coercivity is in agreement with the results of Pasko *et al.*,³⁰ who attributed this drop to the reaction of BaM and spinel phases to form the W-phase at temperatures higher than 1200° C. Further, the transition from a hard magnet ($H_c \sim 2800$ Oe at 1100° C) to a soft magnet ($H_c \sim 300$ Oe at 1300° C) could be associated with the reported spin reorientation transition from easy axis to easy plane in W-type hexaferrite. However, such transition in our sample should be confirmed by other techniques in a future work. In addition, the squareness ratio of 0.53 for the sample sintered at 1100° C is consistent with single-domain particles randomly oriented. However, the decrease in squareness ratio at higher sintering temperatures is indicative of multi-domain particles due to particle growth at such high temperatures³⁰. This multidomain structure typically results in a reduction of the coercivity³.

CONCLUSIONS

Barium hexaferrite phases were synthesized by high energy ball milling and subsequent sintering at temperatures 100, 1200, and 1300° C. Mo-Zn substitution for F^{3+} ions was found to result in a decrease in saturation magnetization due to the presence of secondary impurity oxide phases in samples sintered at 1100° C. Samples sintered at higher temperatures showed an increase in saturation magnetization and a drastic drop in coercivity. The proposed spin reorientation transition at room temperature in the sample with $x = 0.2$ sintered at 1300° C suggests that this sample has a potential application in magnetic refrigeration³⁰. However, this transition should be confirmed by other techniques.

ACKNOWLEDGEMENTS

This work was supported by a generous grant from the Deanship of Scientific Research at The University of Jordan (Grant No. 1404). Thanks are due to Yousef Abu Salha and Waddah Fares (The University of Jordan) for their valuable technical assistance in XRD and SEM data collection.

REFERENCES

1. B.D. Cullity and C.D. Graham, *Introduction to Magnetic Materials*, 2nd ed. (Wiley, Hoboken, NJ) (2009).
2. J. Smit and H.P.J. Wijn, *Ferrites*, (Philips Technical Library, Eindhoven) (1959).
3. *Ferromagnetic Materials*, Vol. 2, E.P. Wohlfarth, ed. (North-Holland, Amsterdam, 1980).
4. R.C. Pullar, Hexagonal ferrites: A review of the synthesis, properties and applications of hexaferrite ceramics, *Progress in Materials Science* **57**: 1191 – 1334 (2012).
5. U. Ozgur, Y. Alivov, and H. Morkoc, Microwave Ferrites, Part 1: Fundamental Properties, *Journal of Materials Science: Materials in Electronics* **20**: 789 – 834 (2009).
6. B. Ul-Ain, S. Ahmed, and Y. Huang, Catalytic decomposition of N_2O on cobalt substituted barium hexaferrites, *Chinese Journal of Catalysis* **34**: 1357-1362 (2013).
7. T. Tanaka, T. Jitoshio, and K. Yamamori, Overwrite and bit shift characteristics of Ba-ferrite floppy disks, *Journal of Magnetism and Magnetic Materials* **134**: 390 – 394 (1994).
8. D.E. Speliotis, Advanced MP⁺⁺ and BaFe⁺⁺ tapes, *Journal of Magnetism and Magnetic Materials* **155**: 83-85 (1996).
9. Z. Yang, C.S. Wang, X.H. Li, and H.X. Zeng, (Zn, Ni, Ti) substituted barium ferrite particles with improved temperature coefficient of coercivity, *Materials Science and Engineering B* **90**: 142-145 (2002).
10. I.V. Zavislyak, M.A. Popov, and G. Srinivasan, A cut-off millimeter wave resonator technique for mapping magnetic parameters in hexagonal ferrites, *Measurement Science and Technology*. **20**: 115704 (5pp) (2009).
11. M. Drogenik, I. Ban, D. Makovec, A. Znidarsic, Z. Jaglicic, and D. Hanzel, The hydrothermal

- synthesis of super-paramagnetic barium hexaferrite particles, *Materials Chemistry and Physics* **127**: 415 – 419 (2011).
12. C. S. Kim, S. W. Lee, and S. Y. An, Mössbauer studies of ($\text{BaFe}_{11.9}\text{Mn}_{0.1}\text{O}_{19}$) by a sol–gel method, *Journal of Applied physics* **87**: 6244-6246 (2000) .
 13. Z. Haijun, L. Zhichao, M. Chengliang, Y. Xi, Z. Liangying, and W. Mingzhong, Complex permittivity, permeability, and microwave absorption of Zn- and Ti-substituted barium ferrite by citrate sol-gel process, *Materials Science and Engineering* **B96**: 289-295 (2002).
 14. G.H. Dushaq, S.H.Mahmood, I. Bsoul, H.K. Juwhari, B. Lahlouh, and M.A. AlDamen, Effects of Molybdenum concentration and valence state effects on the structural and magnetic properties of $\text{BaFe}_{11.6}\text{Mo}_x\text{Zn}_{0.4-x}\text{O}_{19}$ hexaferrites, *Acta Metallurgica Sinica* (English letters) **26**: 509-516 (2013).
 15. J. Qiu, M. Gu, and H. Shen, Microwave absorption properties of Al- and Cr-substituted M-type barium hexaferrite, *Journal of Magnetism and Magnetic Materials* **295**: 263–268 (2005).
 16. I. Bsoul, S. H. Mahmood, and A. Lehlooh, Structural and magnetic properties of $\text{BaFe}_{12-2x}\text{Ti}_x\text{Ru}_x\text{O}_{19}$, *Journal of Alloys and Compounds* **489**: 157–161 (2010).
 17. P. Sharma, R.A. Rocha, S.N de Medeiros, and A. Paesano Jr, Structural and magnetic studies on barium hexaferrites prepared by mechanical alloying and conventional route, *Journal of Alloys and Compounds* **443**: 37 – 42 (2007).
 18. A.Gonzalez-Angeles, G.Mendoza-Suarez, A. Gruskova, J. Slama, J.Lipka, and M. Papanova, Magnetic structure of $\text{Sn}^{2+}\text{Ru}^{4+}$ -substituted barium hexaferrites prepared by mechanical alloying, *Materials letters* **59**: 1815-1819 (2005).
 19. M. Awawdeh, I. Bsoul, and S.H. Mahmood, Magnetic properties and Mössbauer spectroscopy on Ga, Al, and Cr substituted hexaferrites, *Journal of Alloys and Compounds* **585**: 465–473 (2014).
 20. J. Ding, D. Maurice, W.F. Miao, P.G. McCormick, and R. Street, Hexaferrite magnetic materials prepared by mechanical alloying, *Journal of Magnetism and Magnetic Materials*: **150**: 417–420 (1995).
 21. Ding J., Street R., and Nishio H., Magnetic properties of Ba- and Sr-hexaferrite prepared by mechanical alloying, *Journal of Magnetism and Magnetic Materials* **164**: 385-389 (1996).
 22. S. Ounnunkad and P. Winotai, Properties of Cr-substituted M-type barium ferrites prepared by nitrate–citrate gel-autocombustion process, *Journal of Magnetism and Magnetic Materials* **301**: 300-301 (2006).
 23. S. Ounnunkad, Improving magnetic properties of barium hexaferrites by La or Pr substitution, *Solid State Communication* **138**: 472-475 (2006).
 24. S.R. Janasi, D. Rodrigues, F.J.G. Landgraf, and M. Emura, Magnetic properties of coprecipitated barium ferrite powders as a function of synthesis conditions, *IEEE Transactions on Magnetics* **36**: 3327 – 3329 (2000).
 25. S.R. Janasi, M. Emura, F.J.G. Landgraf, and D. Rodrigues, The effects of synthesis variables on the magnetic properties of coprecipitated barium ferrite powders, *Journal of Magnetism and Magnetic Materials* **238**: 168–172 (2002).
 26. D. Mishra, S. Anand, R.K. Panda and R.P. Das, X-ray diffraction studies on aluminum-substituted barium hexaferrite, *Materials letters* **58**: 1147-1153 (2004).
 27. I. Bsoul and S.H. Mahmood, Magnetic and structural properties of $\text{BaFe}_{12-x}\text{Ga}_x\text{O}_{19}$ nanoparticles, *Journal of Alloys and Compounds* **489**: 110-114 (2010).
 28. R.D. Shannon, Revised effective ionic radii and systematic studies of interatomic distances in halides and chalcogenides, *Acta Crystallographica* **A32**: 751 (1976).
 29. B.E. Warren, X-ray Diffraction, (Addison-Wesley, Reading, Massachusetts) (1969).
 30. A. Pasko, F. Mazaleyrat, M. LoBue, V. Loyau, V. Basso, M. Kupferling, C.P. Sasso, and L. Bessais, Magnetic and structural characterization of nanosized $\text{BaCo}_x\text{Zn}_{2-x}\text{Fe}_{16}\text{O}_{27}$ hexaferrite in the vicinity of spin reorientation transition, *Journal of Physics: conference series* **303**: 012045 (6 pp) (2011).
 31. Y.Y. Meng, M.H. He, Q. Zeng, D.L. Jiao, S. Shukla, R.V. Ramanujan, Z.W. Liu, Synthesis of barium ferrite ultrafine powders by sol–

- gel combustion method using glycine gels, *Journal of Alloys and Compounds* **583**: 220 – 225 (2014) .
32. U. Topal, H. Ozkan, K.G. Topal, Improved properties of $\text{BaFe}_{12}\text{O}_{19}$ prepared by ammonium nitrate melt technique and washed in HCl, *Journal of Alloys and Compounds* **422**: 276–278 (2006).
33. Mahmood, S.H., *et al.*, Magnetic Properties and Hyperfine Interactions in M-Type $\text{BaFe}_{12-2x}\text{MoxZnxO}_{19}$ Hexaferrites. *Journal of Applied Mathematics and Physics*, **2**: 77-87 (2014). <http://dx.doi.org/10.4236/jamp.2014.25011>